

## CHAPTER IV: DATASETS, PROCESSING, AND METHODS

This chapter will describe briefly the datasets and processing methods applied in this study, sorted by relevance. The datasets are provided in raster or in ASCII-format. They were analyzed by means of programs and tools developed at the German Aerospace Center (DLR), running in the development environments of VICAR (Video Image Communication And Retrieval), ISIS (Integrated Software for Imagers and Spectrometers), and IDL (Interactive Data Language). These programmes were used to search, download, and view the data, as well as to transform, grid, create subsets or mosaics, colourize, and to take profiles.

Parts of the spectral analysis were done by using the software ENVI, enabling to view the data, take spectra, and calculate spectral ratios. All datasets were combined and overlain onto each other in a GIS with the help of the software ArcGIS by ESRI, providing the ability to analyse and interpret the data in a combined manner. Further statistical analyses and profile visualization were accomplished by using Microsoft Excel. Utilised operating systems were LINUX and Microsoft Windows.

### 4.1 HRSC Data

The High Resolution Stereo Camera (HRSC) on Mars Express is a multi-sensor push broom instrument, which delivers images of the Martian surface and atmosphere at various spatial resolutions<sup>2</sup>. The camera has nine parallel-mounted CCD line sensors operating at different angles of view. This permits the near-simultaneous acquisition of high-resolution, stereo, multi-colour, and multi-phase superimposed image swaths [Jaumann *et al.*, 2007]. Detectors are orientated perpendicular to the orbit track, each with 5184 pixels [Neukum and Jaumann, 2004; Neukum *et al.*, 2004b]. The imaging principle is shown in Fig. 14. The four colour line sensors cover a spectral range from 440 to 970 nm. Five panchromatic channels are used to determine photometric surface characteristics from which digital terrain models (DTMs) are created. Additionally, a super resolution channel (SRC) provides frame images in the one-meter resolution range which are nested in the HRSC swath [Neukum and Jaumann, 2004; Jaumann *et al.*, 2007]. Thanks to its imaging, stereo, photometry, and colour capabilities, the HRSC camera can reveal land forms, physical surface characteristics, topography and composition units, and clouds [Neukum *et al.*, 2004b; Jaumann *et al.*, 2007]. SRC images can be used for detailed photogeological investigations.

---

<sup>2</sup> © Copyright for all HRSC data used and presented in this study: ESA/DLR/FUB (G. Neukum).

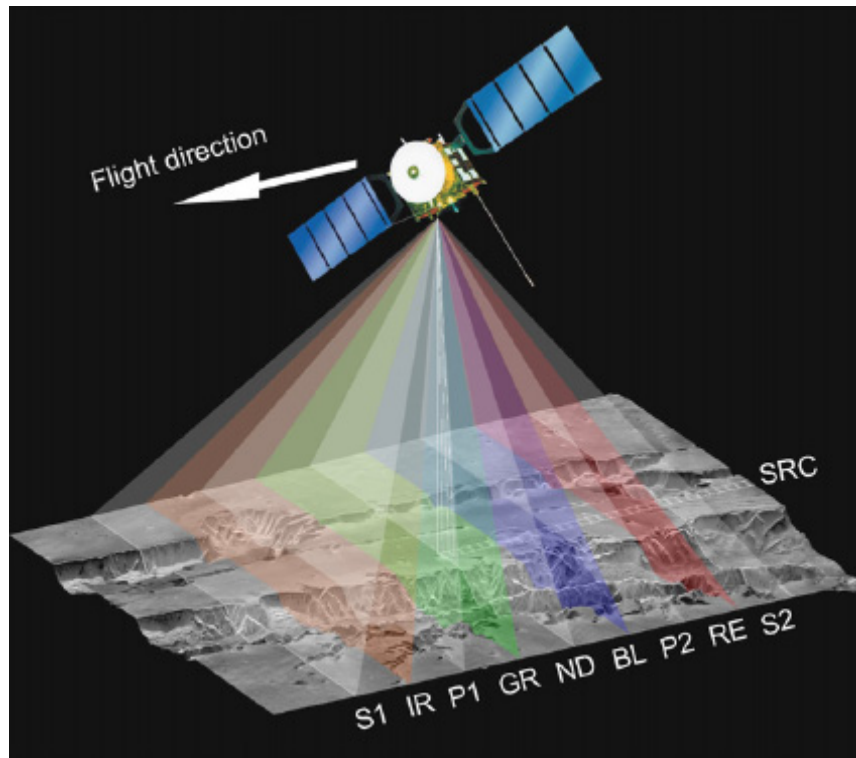


**Figure 14:** HRSC operating principle and viewing geometry of the CCD sensors [Jaumann *et al.*, 2007].

The nadir (ND) and the super-resolution channel (SRC) are located in the middle of the array, surrounded by the green (GR) and blue (BL) channels. P1 and P2 indicate the two photometry channels, followed by near-infrared (IR) and red (RE). The external channels are the stereo channels S1 and S2.

HRSC image data form the basis of the crater database. Because of their spatial resolution of 12.5 m they provide excellent overview images showing the entire craters with a satisfactory resolution of ground details. The use of radiometrically and geometrically calibrated data made further systematic processing unnecessary except for the creation of subsets for every location and mosaics in places where huge craters could not be covered by one HRSC orbit alone.

#### 4.1.1 Selection of Appropriate Craters – The Areas Investigated

The analysis of global dark material focuses on the deposits inside Martian impact craters. Impact craters differ from other depressions because they were caused by the impact of a projectile, which usually results in a circular shape. The first reason for this type of investigation areas is that impact craters act as accumulation sites for the dark material. Although dark material can be found outside of craters as well (cf. Sect. 3.4), these depressions are the primary accumulation site for dark material. On crater floors, the material usually creates dune fields, which are interesting objects of investigation. The second reason is that there is a need for a spatial definition of research areas in the context of a global analysis.

The choice of impact craters is mainly driven by the coverage of high-resolution HRSC data. More than 95 % of the HRSC nadir image data used has a spatial resolution of 12.5 m. For the remaining localities, only 25-m data are available. Another criterion for

data selection was quality. Images of craters located at high latitudes are often affected by atmospheric dust, and thus they were neither useable for any visual analysis nor was it possible to derive reliable digital terrain information from these images. However, terrain information is needed to derive crater profiles for estimating information about the elevation and extent of the deposition sites. The craters selected are located between the latitudes of 70°N and 70°S. Not all the localities chosen are impact craters. Exceptions include one probable collapse depression in Ophir Planum (-2.9°S, 307.8°E, north of Valles Marineris) and the dune field in the caldera of the Nili Patera volcano (-8.8°S, 67.3°E, Syrtis Major). The global distribution of all localities is shown in Fig. 15.

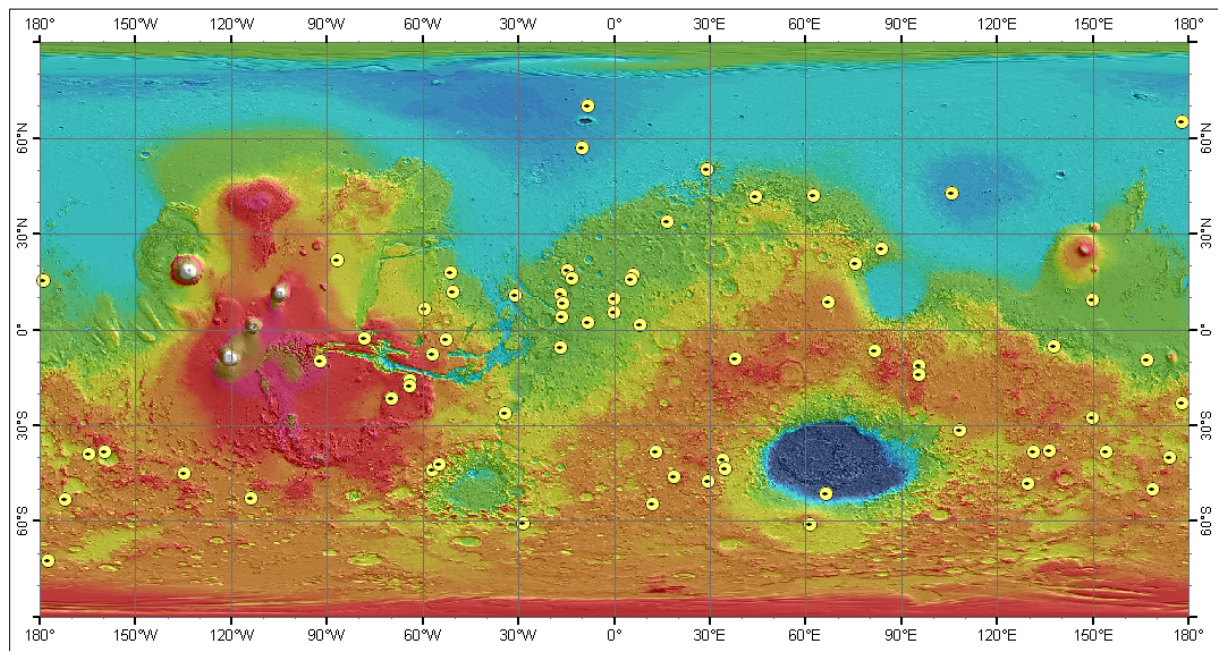


**Figure 15:** Global locations of the 70 areas investigated (background: MOLA topography map).

The localities selected feature the whole range of morphological appearances of dark material such as clusters of single dunes, huge dune fields, and thin sand sheets (see Sect. 3.3). In some places, a mixture of these morphological appearances (e.g. dune fields associated with sand sheets) can be observed. Dark dunes obviously exhibit a great variety of shapes, which will be discussed in detail in Sect. 5.3. Moreover, the craters where dark material is found also differ greatly in type. They include large, degraded craters, craters with central peaks, very young and fresh craters, as well as craters with ejecta blankets (rampart<sup>3</sup> and pedestal<sup>4</sup> craters). A summarizing description of the whole database is given in Sect. 4.8.

<sup>3</sup> Rampart craters have a distinctive splash-like primary ejecta blanket, which probably indicates that their configuration is attributable either to subsurface ice vaporization/fluidization [Carr *et al.*, 1977; Wohletz and Sheridan, 1983], or to aerodynamic effects of the Martian atmosphere [Schultz and Gault, 1979; Barnouin-Jha and Schultz, 1998].

<sup>4</sup> Pedestal craters have erosion-modified ejecta blankets, formed in ice-rich mantle material. Erosion-resistant ejecta blankets may cause craters and ejecta to rise above the terrain elevation. They are most often considered to be the result of ejecta armouring and subsequent deflation [McCauley, 1973; Arvidson *et al.*, 1976].

## 4.2 Visual Interpretation of MOC Data

In places where higher resolution imagery is needed, data from the Mars Orbiter Camera (MOC) are used. This camera was on board the Mars Global Surveyor mission launched in 1996. From 1997 to 2006, the three-component camera delivered horizon-to-horizon images taken by two wide-angle cameras (WA) and high-resolution narrow north-south stripes taken by a narrow-angle camera (NA). The instrument uses the 'push broom' system, meaning that the spacecraft sweeps its field of vision (FOV) across the surface, acquiring one line at a time [Malin and Edgett, 2001]. The wide-angle cameras observe the surface in the red and blue wavelengths (575-625 nm and 400-450 nm) with a spatial resolution of down to 230 m/pixel at the nadir and 1.5km at the limb [Malin et al., 1998; Malin and Edgett, 2001]. These global and regional images can be acquired on every orbit and are thus particularly useful for studying time-variable features such as polar ice caps, lee clouds, and wind streaks. The narrow-angle camera provides images of down to 1.5 m/pixel, which may be used to study geologic and geomorphologic processes such as sediments, sedimentary/polar processes and deposits, and volcanism [Malin et al., 1992].

The MOC images<sup>5</sup> used in this study are narrow-angle images with a spatial resolution of 2.8 m/pixel. The data were downloaded from the Malin Space Science Systems web page ([www.msss.com/mgs/moc/index.html](http://www.msss.com/mgs/moc/index.html)), transformed into VICAR format, and map-projected to equidistant projection in order to fit onto the HRSC data sets. Images were visually interpreted to recover detail information such as dune types and exposed dark layers in crater walls. Fig. 16 shows MOC images superimposed on HRSC orbits, demonstrating the increase in detail information gained by the use of MOC data.

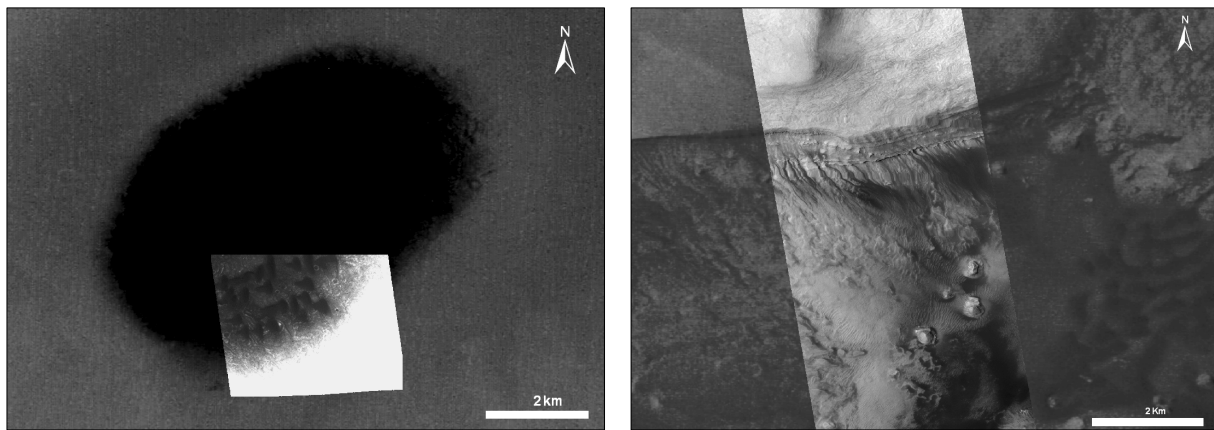


**Figure 16:** MOC images (2.8 m/pixel) overlaid on HRSC (12 m/pixel) images revealing morphological details. **Right:** MOC S05019074 overlaid on HRSC 1323\_0000 showing barchan dunes at a dark patch in Fesenkov Crater (21.9°N, 273.5°E). **Left:** MOC E1100389 on HRSC 4280\_0000 revealing dark gullies emanating from a dark layer exposed in the wall of a pit at Rabe Crater (44.0°S, 34.7°).

<sup>5</sup> © Copyright for all MOC images used and presented in this study: NASA/JPL/Malin SpaceScienceSystems.



### 4.3 Derivation of Brightness Temperature from THEMIS Data

In 2001, the thermal emission imaging system (THEMIS) was launched on board the Mars Odyssey orbiter to investigate the surface mineralogy and physical properties of Mars. Since February 2001, it has been providing day and night multi-spectral thermal infrared images with a resolution of 100 m per pixel, one-band visible images with a highest spatial resolution of 18 m per pixel, and a small number of visible-colour images having five bands. The thermal infrared images have nine channels centred from 6.8 to 14.9  $\mu\text{m}$ , whereas the visible/near-infrared images have five bands centred from 0.42 to 0.86  $\mu\text{m}$  [Christensen *et al.*, 2004a]. Research activities using THEMIS data aimed to determine the mineralogy and petrology of particular deposits associated with hydrothermal or sub-aqueous environments, and to search for thermal anomalies associated with active sub-surface hydrothermal systems. Further scientific objectives included studying small-scale geologic processes and landing site characteristics on the basis of morphologic and thermophysical properties and investigating the polar caps [Christensen *et al.*, 2004a]. A multi-spectral micro bolometer array was used to acquire infrared data with an image width of 23 km. This focal plane has 320 cross-track pixels and 240 down-track pixels [Ferguson *et al.*, 2006a]. 10 narrow-band stripe filters produce  $\sim 1 \mu\text{m}$  wide bands at nine different wavelengths [Christensen *et al.*, 2004a].

The THEMIS data<sup>6</sup> used in this study are night-time infrared images with a spatial resolution of 100m. The data were downloaded from the THEMIS data release web site (<http://themis-data.asu.edu/>). The brightness temperature record (BTR) data product was used, which is derived from band 9 of a radiometrically calibrated (RDR: reduced data record) THEMIS infrared cube (<http://themis-data.asu.edu/pds/document/sdpsis.pdf>).

The raw BTR data show grey values from 0-255, with bright tones representing higher temperatures and dark tones corresponding to lower temperatures. The grey values of these images were converted into temperatures by replacing the 0-255 grey-scale range by the minimum and maximum BTR range of the individual images. These values were derived from the label files of the images. Fig. 17 shows the transformation from grey-scale to colour-coded surface brightness temperature images. While the grey-scale images already display the relative temperature difference between the dunes and their surroundings, only the colour-coded BTR images provide the absolute night-time surface brightness temperature values for the observed regions. These data were acquired and processed for every crater location. For the measurement of temperature values, only summertime THEMIS data were used in order to avoid any thermal influence by possible ice layers. THEMIS mosaics consist of data from different seasons and reflect normalised temperature values.

---

<sup>6</sup> © Copyright for all THEMIS images used and presented in this study: NASA/JPL/ASU.

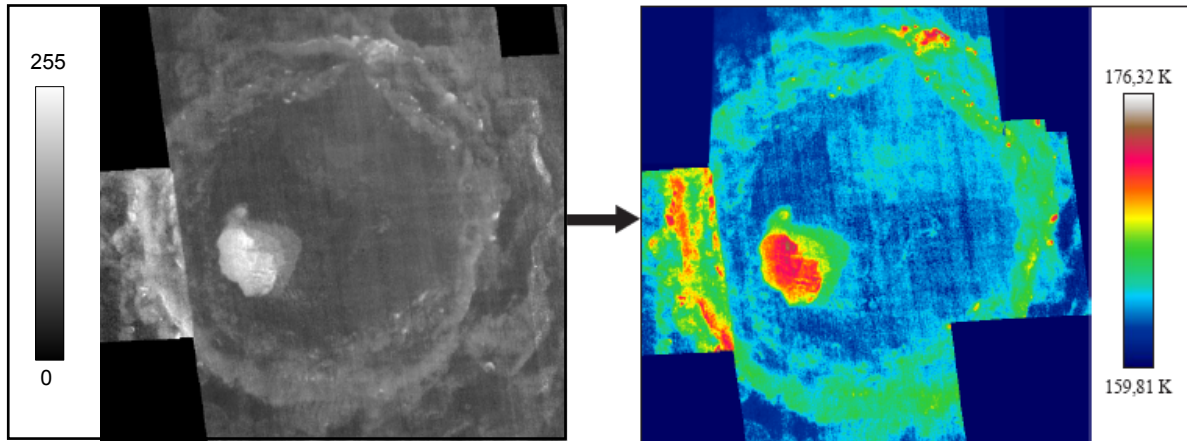


**Figure 17:** Comparison of THEMIS grey-scale image and transformed BTR colour image of a crater at 15.5°N, 181.5°E

**Left:** THEMIS grey-scale mosaic of I04594022, I06816025, I0889007, I15128029, and I16950027. Bright tones indicate warmer and dark tones cooler regions. **Right:** THEMIS-BTR-mosaic of I04594022, I06816025, I08289007, and I15128029. Temperatures are colour-coded and can be read from the legend.

## 4.4 TES Data - Thermal Inertia Derivation and Theoretical Background

Since 1997, the thermal emission spectrometer (TES) on board the Mars Global Surveyor (MGS) has been providing data for studying the atmosphere and surface of Mars. The experiment is designed to address multiple scientific objectives using thermal infrared spectroscopy (between 5.8 and 50  $\mu\text{m}$ ) together with broadband thermal and solar reflectance radiometry (5.1-150  $\mu\text{m}$  and 0.3-2.9  $\mu\text{m}$ , respectively) [Christensen *et al.*, 1998; Christensen *et al.*, 2001]. The mineralogical mapping of Mars, the study of the Martian dust and clouds, the polar caps and the thermophysical properties (e.g. thermal inertia) of the Martian surface belong to the main targets of this mission. The instrument consists of three parts: a Michelson interferometer, a bolometric thermal radiance spectrometer, and a solar reflectance spectrometer gathering data with a spectral resolution of  $\sim 5$  and  $10 \text{ cm}^{-1}$ , a radiometric resolution of  $> 400$  (S/N-ratio at  $1000 \text{ cm}^{-1}$  and  $270 \text{ K}$ ) and a spatial resolution of up to 3 km [Christensen *et al.*, 1998; Christensen *et al.*, 2001].

For the analysis of dune surface conditions, thermal inertia is used because it is the key surface property determining the diurnal and seasonal variation of surface temperatures and is most closely related to the thermal conductivity of a surface [Jakosky and Christensen, 1986]. Materials of different density show a different response to temperature variations. Therefore, thermal inertia (abbreviation: TI) can be used to determine physical properties of surface materials, such as grain size and degree of induration, as well as the abundance of rocks and the exposure of bedrocks [Mellon *et al.*,

2000; *Christensen et al.*, 2001; *Pelkey et al.*, 2001; *Putzig and Mellon*, 2007b]. It reflects the thermal properties of a subsurface within the top few centimetres (i.e. the thermal skin depth, see Sect. 5.5.1) [*Putzig*, 2006].

The thermal inertia is defined as

$$I = \sqrt{\kappa \rho c} \quad (3)$$

where  $\kappa$  is bulk thermal conductivity,  $\rho$  is bulk density, and  $c$  is specific heat capacity [*Putzig and Mellon*, 2007a]. The density and specific heat of geologic materials vary only by a factor of 3, and conductivity varies by 3–4 orders of magnitude under Martian conditions [*Wechsler and Glaser*, 1965; *Edgett and Christensen*, 1991; *Presley and Christensen*, 1997a; *Ferguson et al.*, 2006a]. Thus, conductivity has the strongest influence on thermal inertia. This heat transfer is influenced by several material parameters, such as particle size, particle shape, particle size sorting, and material bulk density [*Presley*, 2002]. The thermal conductivity of materials is a function of solid conduction, radiative transfer through grains and across pores, and gas conductivity [*Palluconi and Kieffer*, 1981; *Ferguson et al.*, 2006a]. Solid and radiative conductivities have a small influence under Martian temperatures, whereas gas conduction plays an important role in the transfer of thermal energy [*Palluconi and Kieffer*, 1981; *Presley and Christensen*, 1997b]. The latter depends on the proportion of gas-gas molecule collision to gas-grain collision. Thus, it is largely controlled by the pore size and the particle size relative to the mean free path of a gas ( $\sim 4.4 \mu\text{m}$  at Martian pressures) [*Palluconi and Kieffer*, 1981; *Edgett and Christensen*, 1991; *Pelkey et al.*, 2001; *Ferguson et al.*, 2006a].

If particles are large, the mean free path is equal to or smaller than the pore size so that gas-gas collisions dominate, resulting in an efficient heat transfer, i.e. in a high thermal conductivity. In this case, gas conduction is independent from pressure and particle size [*Palluconi and Kieffer*, 1981; *Pelkey et al.*, 2001]. If grains are small, the mean free path is much larger than the pore size, gas-gas collisions become rare, and the gas molecules move unimpeded between the grains. In this case, grain-to-grain contact increases, resulting in inefficient heat transfer and low gas conduction [*Jakosky*, 1986; *Ferguson et al.*, 2006a]. In this case, gas conduction varies approximately linearly with the pressure [*Palluconi and Kieffer*, 1981]. At low pressures (that is, under Martian conditions), thermal conductivity is roughly proportional to the square root of the particle diameter, while at high pressures, dependence on the collision between gas molecules increases and the thermal energy transfer becomes independent from the particle diameter [*Wechsler and Glaser*, 1965; *Palluconi and Kieffer*, 1981; *Jakosky*, 1986; *Presley and Christensen*, 1997b].

In summary, thermal conductivity increases with increasing particle size [*Presley and Christensen*, 1997b]. This relationship clearly demonstrates that thermal inertia, which comprises thermal conductivity, is strongly controlled by particle size and can be related to the effective particle size of unconsolidated granular materials under Martian conditions (see Sect. 5.5.3) [*Edgett and Christensen*, 1994].

Traditionally, thermal inertia has been given in units of  $\text{cal cm}^{-2} \text{K}^{-1} \text{s}^{-1/2}$  or  $10^3 \text{cal cm}^{-2} \text{K}^{-1} \text{s}^{-1/2}$ . More recently, the SI unit of  $\text{J m}^{-2} \text{K}^{-1} \text{s}^{-1/2}$  has been established and will be used for every thermal inertia value hereinafter.

The data used in this work<sup>7</sup> have been computed by the TES team of Arizona State University (ASU) and downloaded from the data archive web site ([http://tes.asu.edu/data\\_archive.html](http://tes.asu.edu/data_archive.html)). They use a thermal model of Mars similar to that of *Harberle & Jakosky* (1991) to derive surface kinetic and planetary brightness temperatures from the emitted infrared energy measured by TES. These temperatures are driven by several factors such as thermal inertia, albedo, surface pressure, and atmospheric dust opacity. The surface thermal inertia of the top 1-10 cm is derived from a lookup table covering a variety of physical conditions and the corresponding local time of day, season, and latitude [*Christensen et al.*, 1998; *Mellon et al.*, 2000; *Putzig et al.*, 2005; *Christensen*, 2006]. In other words, the thermal inertia is determined by comparing the measured infrared brightness temperature of the surface at many different times of day with temperatures predicted with the thermal model [*Haberle and Jakosky*, 1991; *Jakosky et al.*, 2000].

Parts of this comprehensive ASU TES data product were acquired for every crater location, including thermal inertia, albedo, surface pressure, brightness and surface temperature, acquisition time and date, orbit number, and several auxiliary acquisition parameters. Only those TI values were extracted from the collected TES data sets, which met several minimum quality requirements: a maximum emission angle of  $3^\circ$ , a maximum quality bolometric inertia rating of 1, and a maximum quality bolometer lamp anomaly of 1. Furthermore, only night-time thermal inertia values between 24 and  $800 \text{ J m}^{-2} \text{K}^{-1} \text{s}^{-1/2}$  were used. Thermal inertia is most reliable at night when thermal contrasts due to variations in slope and emissivity are reduced and particle size effects are enhanced [*Edgett and Christensen*, 1994]. These values were extracted and gridded for every crater location to derive colour images for presentation (Fig. 18, left). However, only ungridded single-point measurements from the summer season were used for the analysis itself (Fig. 18, right). The tool for data extraction and incorporation in the GIS was developed by [*Saiger*, 2008]. Summertime data were used to avoid measured values being corrupted by a possible  $\text{CO}_2$  or  $\text{H}_2\text{O}$  frost layer on the dune surfaces. Moreover, these single-point measurements permitted pointing directly at a dune to minimize the disadvantage of the spatial resolution of 3 by 3 km per pixel, which is inappropriate for such small morphologies. Nevertheless, it could not always be avoided to have TI values that corresponded not only to the dune surfaces but also to parts of the surroundings in places where the dunes are very small. In these cases, caution is required in interpreting the results.

---

<sup>7</sup> © Copyright for all TES data used and presented in this study: NASA/JPL/ASU



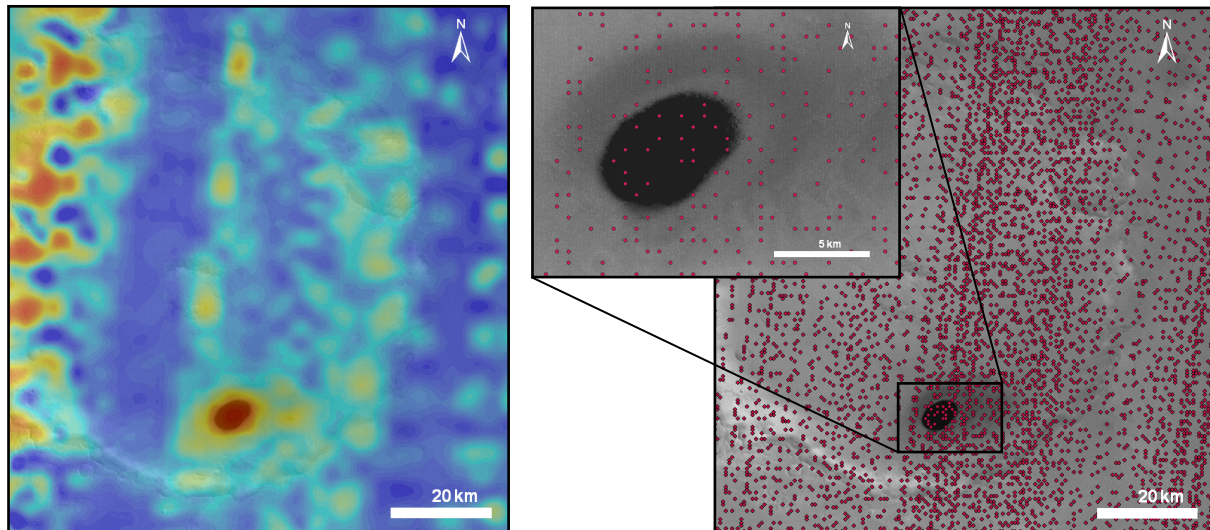


**Figure 18:** Comparison of gridded (**left**) and ungridded (**right**, [Saiger, 2008]) TES data overlaid on HRSC 1223\_0000.

The gridded data are interpolated for display by a cubic convolution resampling method. The stripy textures of the higher values on the left-hand image margin are artefacts of TI data processing [Mellon *et al.*, 2000].

## 4.5 Spectral Analysis of OMEGA Data

Since December 2003, the visual–infrared mapping spectrometer OMEGA (Observatoire pour la Minéralogie, l’Eau, les Glaces, et l’Activité [Bibring *et al.*, 2004]) on board the European mission Mars Express has been mapping the surface composition of Mars. The instrument operates in a spectral range of 0.38–5.1  $\mu\text{m}$  and produces hyperspectral reflectance imagery with a spatial resolution of 0.3 to 5 km and 352 spectral channels. The combination of spectroscopy and imagery allows performing interdisciplinary scientific investigations such as studying the surface mineralogy (minerals of the major geologic units such as silicates, carbonates, oxides and hydrates), the polar ice caps and frost (spatial evolution, observation of  $\text{CO}_2$  and  $\text{H}_2\text{O}$  ice), and the molecular composition and parameters of the atmosphere (total pressure, column densities of the minor constituents  $\text{H}_2\text{O}$  and  $\text{CO}$ , content of aerosols) on Mars [Bellucci *et al.*, 2004; Bibring *et al.*, 2004; Bibring *et al.*, 2005].

The mineralogical composition of the dark material was examined with the aid of near-infrared OMEGA spectral reflectance data<sup>8</sup> from 1–2.5  $\mu\text{m}$ , where most minerals exhibit diagnostic absorption bands. The radiance data were corrected for atmospheric absorption and solar irradiance using standard reduction schemes described by Bellucci *et al.* (2006) and Bibring *et al.* (2006). Atmospheric correction of the spectral data is necessary because

<sup>8</sup> © Copyright for all OMEGA data used and presented in this study: ESA/IAS.

observations of surface reflectance also include atmospheric contributions from dust, water vapour, water-ice aerosols, and CO<sub>2</sub> [Mustard *et al.*, 2005]. The correction method applied assumes a multiplicative impact of surface and atmospheric influences on the spectra, which follows a power law variation with altitude. The correction was done by means of an atmospheric reference spectrum created from high-resolution OMEGA measurements crossing the base and the summit of Olympus Mons. Assuming a constant surface contribution, the ratio of base to summit spectrum will result in an atmospheric spectrum as a power function of different altitudes [Mustard *et al.*, 2005]. This correction spectrum was kindly provided by François Poulet, a member of the OMEGA science team at the Institut d'Astrophysique Spatiale of the Université Paris-Sud. In order to eliminate atmospheric influences, all spectra analyzed were divided by the correction spectrum, taking into account the strength of CO<sub>2</sub> atmospheric absorption measured in the observation. The data correction procedure generates reflectance I/F (ratio of observed radiance to incoming solar flux per surface unit [Poulet *et al.*, 2007]) spectra, which reliably reflect the intrinsic properties of the surface. Prior to the atmospheric correction, all OMEGA data sets were geometrically corrected by applying an IDL routine developed at DLR by members of the Mars Express Operation Team. The OMEGA data used for this study have different spatial resolutions, which range from 300 m to 3 km, depending on the size of the respective dune field or sand sheet as well as on data availability.

#### 4.5.1 Mineral Detection - The Ratio Technique

The theory behind the determination of minerals or mineral mixtures by spectral analysis is that crystal-lattice vibrations in minerals modify the spectral signal from surfaces in distinct ways [e.g. Burns, 1970; Adams, 1975; Pieters, 1977; McCord and Clark, 1978; Mustard, 2002; Bonello *et al.*, 2004]. In the ultraviolet, visible, or infrared portions of the spectrum, minerals have regions of strong absorption [Adams, 1975; Bell *et al.*, 1975; Lucey and Clark, 1984]. This work focuses on the detection of minerals by analyzing their reflectance properties in the near infrared wavelength range.

For mineral detection, an IDL routine was used that applies a ratio technique to geometrically and atmospherically corrected OMEGA data. This technique was developed and described in detail by Poulet *et al.* (2007). The spectral parameters (also referred to as spectral indices or spectral criteria in the following) used for mineral detection were also obtained from Poulet *et al.* (2007) and are listed in Table 4. Absorption bands occur when a certain mineral absorbs incoming sunlight. Absorption bands that are characteristic for a certain mineral are identified by building the ratio of the reflectance values at the bottom (centre) and the shoulder position (continuum) of the desired absorption band [Clark and Roush, 1984]:

$$D = 1 - R_b / R_c \quad (4)$$

where  $D$  is the band depth,  $R_b$  is the reflectance at the absorption centre, and  $R_c$  is the reflectance of the continuum. Detection thresholds for each mineral absorption are defined to keep the signal level significantly above instrumental noise and atmospheric artefacts [Poulet *et al.*, 2007]. These thresholds ensure that all spectral artefacts caused by instrumental noise, observation geometry and atmospheric effects will be taken into account. The threshold values represent the point at which the depth of absorption is equal to or higher than the noise in the spectrum. Absorption bands that are smaller in depth than the noise will not be used for interpretation. Based on former studies, it is well known that the regions on Mars which are covered by dark material are dominated by mafic volcanic rock minerals such as pyroxene and olivine [e.g. Christensen *et al.*, 2000; Bibring and Erard, 2001; Bandfield, 2002; Hoefen *et al.*, 2003; Mustard *et al.*, 2005; Bibring *et al.*, 2006; Mangold *et al.*, 2007; Mustard *et al.*, 2007] as well as plagioclase [Christensen *et al.*, 2000].

Therefore, a mafic composition of the dark material was assumed, and mineral detection was a priori employed to look for olivines  $[(\text{Mg,Fe})_2\text{SiO}_4]$  and pyroxenes  $[(\text{Ca,Fe,Mg})_2\text{Si}_2\text{O}_6]$ . The question was whether all examined dark material deposits exhibited this mafic signature or whether there were some localities showing a different spectral signature.

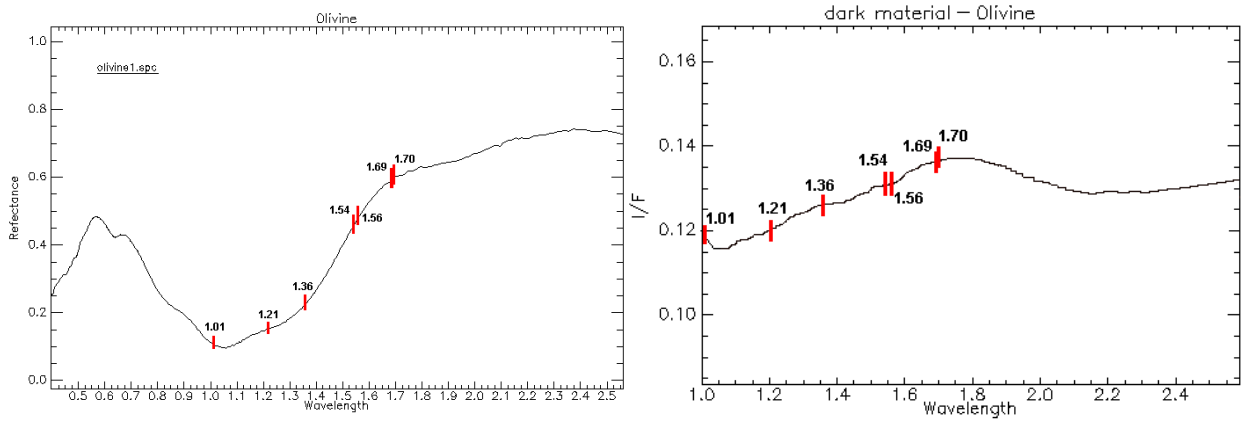
Using two different olivine absorption wavelength criteria (see Tab. 4), the method allows discriminating between magnesium- and iron-dominated olivines, i.e. forsterite and fayalite, respectively. These spectral criteria are based on a reflectance increase from 1.1  $\mu\text{m}$  to higher wavelengths (see Fig. 19), which results from an absorption band shift (between 1.0 to 1.4  $\mu\text{m}$ ) due to increasing occupation of the M2 sites by  $\text{Fe}^{2+}$  [Jaumann, 1989]. The absorptions are caused by the crystal field transition of  $\text{Fe}^{2+}$  ions at non-centrosymmetric M2 sites [Burns, 1970; Adams, 1975]. Bandwidth, shape, and position vary with the Fe content. An absorption band around 1  $\mu\text{m}$  is not a spectral feature that is unique to olivine because many other minerals similarly exhibit absorption in this wavelength range (cf. pyroxene spectrum in Fig. 20). However, other minerals display additional absorption bands at longer or shorter wavelengths. Thus, a detection of olivine can be confirmed if the presence of other absorption bands can be ruled out [Adams, 1975]. Although there are two individual indices for forsterite and fayalite it is difficult to make a reliable spectral discrimination because forsterite with large grain sizes ( $>>100 \mu\text{m}$ ) is spectrally similar to fayalite with small grain sizes [Mustard *et al.*, 2005] (see Sect. 5.3.1.). Since it is not mandatory in this analysis, these two kinds of olivines are not differentiated. For olivines, the detection threshold is 1.04 for forsterite and 1.02 for fayalite to ensure a correct interpretation [Poulet *et al.*, 2007].

A typical spectrum of pyroxene generally has two distinct absorption bands; one narrow and deep band around 0.9 to 1  $\mu\text{m}$  and a second one around 1.8 to 2.3  $\mu\text{m}$  (Fig. 20). Because of the non-uniqueness of the 1- $\mu\text{m}$  band, pyroxene is identified by its broad absorption band around 2  $\mu\text{m}$  and the shape of 1- $\mu\text{m}$  band (for a discussion of possible confusions with  $\text{CO}_2$  around 2  $\mu\text{m}$  see Sect. 5.3.1). The 2- $\mu\text{m}$  absorption arises predominately from the crystal field transition of the  $\text{Fe}^{2+}$  ions on the M2 crystallographic

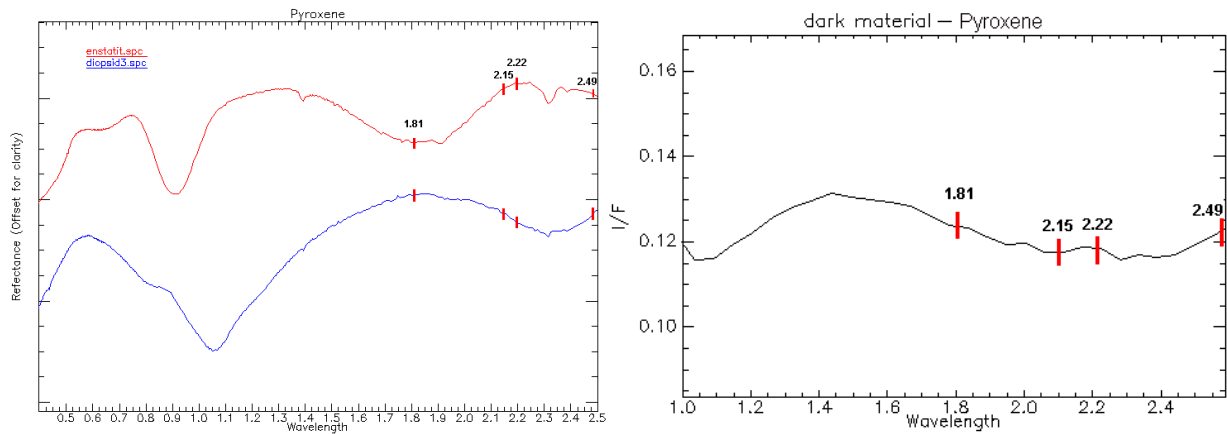
site [Burns, 1970; Adams, 1975; Jaumann, 1989]. The defined ratio for mineral detection is based on the presence of this broad 2  $\mu\text{m}$  band corresponding to a mixture of both high-calcium pyroxenes (HCP, band centre at 1.9  $\mu\text{m}$ ) and low-calcium pyroxenes (LCP, band centre at 2.3  $\mu\text{m}$ ) [Burns, 1970; Adams, 1975; Poulet *et al.*, 2007]. A detection threshold value of 0.1 ensures that the measured spectral features are not caused by instrumental or atmospheric effects. Additionally, the shape of the 1- $\mu\text{m}$  band was checked by viewing the individual spectra. A narrow 1- $\mu\text{m}$  band in association with a 2- $\mu\text{m}$  band points to pyroxene only, whereas a broad 1- $\mu\text{m}$  band associated with a 2- $\mu\text{m}$  band points to a mixture of olivine and pyroxene.

Fig. 19-21 shows laboratory absorption spectra samples of the minerals under discussion. High-calcium pyroxenes are represented by the spectrum of diopside and low-calcium pyroxenes by enstatite. As all common olivines have the same broad 1- $\mu\text{m}$  absorption, only one sample spectrum of an iron-rich olivine is shown here. It should be remembered that the aforementioned minerals are only detectable by their iron content, resulting in only iron-rich/iron-bearing mineral types actually being detected. The wavelength positions of the applied calculations (see Table 4) are indicated by red marks on the laboratory and the sample OMEGA spectra. The spectral criterion of water-bearing minerals was used to analyze whether some parts of the dark material patches have undergone a chemical alteration, such as the physical or chemical absorption of water molecules by hydrated sulphates, hydrous hydroxides and certain phyllosilicates [Poulet *et al.*, 2008]. Hydrated minerals exhibit (besides others) typical vibration features around 1.9  $\mu\text{m}$  (see Fig 20) which are caused by overtones and combinations of OH and H<sub>2</sub>O components in the crystal lattice [Adams, 1975]. These wavelengths were selected because they lie outside the main atmospheric bands [Poulet *et al.*, 2007]. These wavelengths were selected because they lie outside the main atmospheric bands [Poulet *et al.*, 2005]. The detection threshold for hydrated minerals is 0.02. Note that this spectral criterion does not serve for monohydrated sulphates (such as kieserite or romerite) because their corresponding hydration bands are shifted to longer wavelengths (2.1 and 2.4  $\mu\text{m}$ ) [Arvidson *et al.*, 2005; Gendrin, 2005; Poulet *et al.*, 2007; Poulet *et al.*, 2008]. Nevertheless, the aim of this study is not to identify and discriminate between hydrated minerals but to look for any indications of aqueous alteration in terms of the presence of water molecules in the crystal lattice.

Additionally, it was checked with the aid of applicable spectral criteria whether H<sub>2</sub>O ice or CO<sub>2</sub> ice [e.g. Forni *et al.*, 2005] is abundant in the materials (see Table 4). The presence of ice might corrupt the results and interpretation of the detection especially of hydrated minerals [Poulet *et al.*, 2007]. For this reason, localities with H<sub>2</sub>O or CO<sub>2</sub> ice in the dark material were excluded from the detection of hydrated and mafic minerals. See Sect. 5.3.1 for a detailed discussion of uncertainties.



**Figure 19:** Laboratory spectrum derived from the ENVI spectral library (**left**) and OMEGA spectrum (**right**) of olivine with wavelength positions (red marks) used for the spectral criteria calculation (see Table 4).



**Figure 20:** Laboratory spectra of LCP and HCP from the ENVI spectral library (**left**) and OMEGA spectrum (**right**) of pyroxene with wavelength positions (red marks) used for the spectral criteria calculation (see Table 4).

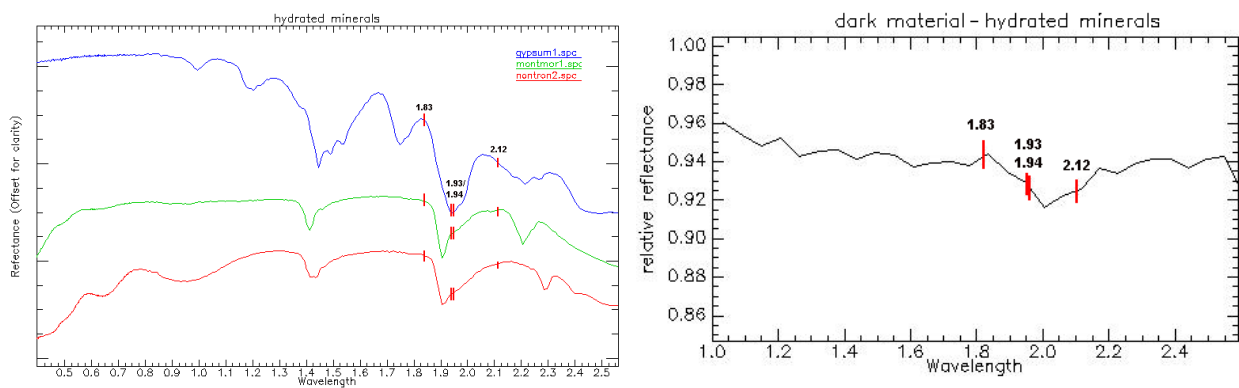


**Figure 21:** Laboratory spectra of different hydrated minerals derived from the ENVI spectral library (**left**) compared to OMEGA spectrum (**right**) of hydrated minerals with wavelength positions (red marks) used for spectral criteria calculation (see Table 4).



**Table 4:** Spectral parameters used for mineral detection with corresponding detection thresholds adapted from *Poulet et al. (2007)*.

Name	Formulation	Detection Threshold	Rationale
NIR albedo	$R(1.08)/\cos(i)$ With $i$ : incidence angle relative to aereoid	N/A	Lambertian Albedo
0.55- $\mu\text{m}$ band depth or $\text{Fe}^{3+}$ parameter	$1-R(0.55)/$ $(0.5 \cdot R(0.44) + 0.5 \cdot R(0.65))$	0	degree of oxidation or amount of dust contamination of the surface
Nanophase ferric oxide or 1/0.8- $\mu\text{m}$ slope	$R(0.97)/R(0.80)$	1	Nanophase ferric oxides if ratio $\geq 1$
Pyroxene	$1-(R(2.15)+R(3.33))/$ $(R(1.81)+R(2.49))$	0.01	2- $\mu\text{m}$ band due to both Low-Calcium and High- Calcium pyroxenes
Forsterite or Mg- rich olivine	$(0.5 \cdot R(1.54) + 0.5 \cdot R(1.56))/$ $(0.1 \cdot R(1.01) + 0.2 \cdot R(1.21) +$ $0.7 \cdot R(1.36))$	1.04	1- $\mu\text{m}$ band due to Mg-rich Olivine
Fayalite or Fe-rich olivine	$(0.5 \cdot R(1.69) + 0.5 \cdot R(1.70))/$ $(0.1 \cdot R(1.01) + 0.1 \cdot R(1.21) +$ $0.4 \cdot R(1.36) + 0.4 \cdot R(1.50))$	1.02	1- $\mu\text{m}$ band due to Fe-rich Olivine and/or large grain size ( $> 1 \text{ mm}$ )
1.9- $\mu\text{m}$ band depth or hydrated mineral	$1-(0.5 \cdot R(1.93) + 0.5 \cdot R(1.94))/$ $(0.5 \cdot R(1.83) + 0.5 \cdot R(2.12))$	0.02	Water-bearing mineral
Water ice	$1-(R(1.50)+R(1.51))/$ $(R(1.30)+R(1.71))$	0	1.5- $\mu\text{m}$ band due to water ice
$\text{CO}_2$ ice	$1-R(1.43)/$ $(0.5 \cdot R(1.38) + 0.5 \cdot R(1.44))$	0	1.43- $\mu\text{m}$ due to $\text{CO}_2$ ice

## 4.6 Additional Orbital Data Sets

The data sets introduced in Sect. 4.1 to 4.5 were compiled and processed for every crater location. At the same time, there were various data from orbital Martian missions, which were not acquired for every location.

Mars Orbiter Laser Altimeter (MOLA) data were used as a base map in the GIS, providing a global shaded relief with elevation information. This MOLA base map forms the background of every global image shown in this work. For certain locations, MOLA elevation information (vertical precision  $<10$  m [Zuber *et al.*, 1998]) is also used as a substitute for HRSC DTMs (vertical accuracy 90 % of the nadir resolution [Gwinner *et al.*, 2005]) when HRSC data provided insufficiently accurate values due to the lack of high-resolution HRSC DTMs.

During the preparation for this work in 2006, a further Mars satellite named Mars Reconnaissance Orbiter (MRO) began to orbit the planet. On board, the high resolution imaging science experiment (HiRISE) and the compact reconnaissance imaging spectrometer for Mars (CRISM) respectively provide high-resolution image and spectral data of extraordinarily high quality and spatial resolution. Detailed instrument descriptions are given by McEwen *et al.* (2007) for HiRISE and Murchie *et al.* (2004), Silverglate and Fort (2004), and Silverglate *et al.* (2004) for CRISM. These image and spectral data sets are so far only acquired for a few localities. HiRISE images with a spatial resolution of 25 cm/pixel provide an impressive insight into the details of dark layers in crater walls and dune morphology. Thanks to CRISM's spatial resolution of 19 m and the spectral range of 0.37 - 3.92  $\mu\text{m}$ , it was possible to derive spectral information on the mineralogical composition of these layers [Pelkey *et al.*, 2007]. The application of these data sets is presented in Sect. 5.2 and 5.3.

Table 5 summarizes all orbital data sets used for this work.

**Table 5:** Overview of all data sets used in this study.

The spatial resolutions given are specifications for the data used in this study, not general ranges.

Dataset	Mission	Data type	Spatial resolution/px	Spectral range/ No° channels	Relevance / coverage
HRSC	Mars Express	Raster (optical image and elevation data)	12.5 - 25 m image data / ~ 50 m DTMs	440 - 970 nm / 4 (colour) + 5 (panchrom.)	data basis, data for every locality
OMEGA	Mars Express	Raster (spectral image data)	300 m - 3 km	0.38 - 5.1 $\mu\text{m}$ / 352	data for every locality, if available
THEMIS	Mars Odyssey	Raster (thermal image data)	100 m	VIS/NIR: 0.42 - 0.86 $\mu\text{m}$ / 5 TNIR: 6.8 - 14.9 $\mu\text{m}$ / 9	data for every locality, if available
TES	Mars Global Surveyor (MGS)	ASCII (thermal data)	3 km	interferometer: 5.8 - 50 $\mu\text{m}$ radiometer: 5.1 - 150 $\mu\text{m}$ and 0.3-2.9 $\mu\text{m}$	data for every locality, if available
MOC	Mars Global Surveyor (MGS)	Raster (optical image data)	2,8 m	wide angle: 575 - 625 nm and 400 - 450 nm	data for every locality, if available
MOLA	Mars Global Surveyor (MGS)	ASCII and raster (elevation data)	vertical precision <10m	-	global base map
CRISM	Mars Reconnaissance Orbiter (MRO)	Raster (spectral image data)	15 - 19 m	0.37-3.92 nm / 438	data for few localities
HiRISE	Mars Reconnaissance Orbiter (MRO)	Raster (optical image data)	25 cm	~536 – ~874 nm / 3 (colour)	data for few localities

## 4.7 Wind Direction Data

Dealing with aeolian bed forms naturally raises the question of wind directions and velocities. Local dune-forming wind patterns can be determined from the shapes and slopes of the observed aeolian bed forms [Greeley, 1985]. These wind patterns deduced from dune morphology will be compared with current model wind data (see Sect. 5.4). For this comparison, modelled wind field data from the Mars climate database (MCD, [Forget *et al.*, 1999; Lewis *et al.*, 1999; Forget *et al.*, 2007]) were used. In former stages of this study, a second modelled wind field data set Mars Global Reference Atmospheric Model (MarsGRAM, [Justus *et al.*, 2002]), was employed in comparing the two records. The data sets differ in spatial resolution. The MCD data are computed for a  $5^\circ$  by  $3^\circ$  grid, whereas the MarsGRAM data have a slightly higher spatial resolution with  $2^\circ$ . However, data retrieval from the latter model was very time-consuming and thus difficult to realize. To augment the crater database, new data were constantly requested which, in the case of the MarsGRAM data, were not supplied as desired. Consequently, it was not possible to obtain a complete modelled wind data set for all localities addressed in this analysis. Whereas the MCD data provided 100 % coverage, the MarsGRAM data set only covered about 60 % of the desired localities. Thus, the analysis was continued with the MCD data set only.

Morphology-deduced wind direction data were created in the GIS (see Sect. 4.7.2) and completed with slip face orientation data from the Mars Global Digital Dune Database (MGD<sup>3</sup>).

### 4.7.1 Modelled Wind Field Data - The Mars Climate Database

The MCD is a database of meteorological fields, which describes the climate and environment of the Martian atmosphere. The data are obtained from improved state-of-the-art general circulation models (GCMs) which are based on physical laws and prescribed parameters [Forget *et al.*, 1999; Lewis *et al.*, 1999]. The models are developed jointly by the Laboratoire de Météorologie Dynamique du Centre National de la Recherche Scientifique (France), the Open University of Oxford (United Kingdom), and the Instituto de Astrofísica de Andalucía (Spain), with the support of the European Space Agency. The parameters provided by the MCD include, for example, atmospheric pressure, density, winds, and temperature; surface pressure and temperature; CO<sub>2</sub> ice cover; thermal and solar radiative fluxes; dust opacity; and many more [Forget *et al.*, 2006; Forget *et al.*, 2007].

The data used for this analysis are version-4.2 data from the dust storm scenario model. The dust storm season was chosen because it is then that sand transport on Mars is most likely. The data were calculated for every crater locality. They have a spatial resolution of  $5.625^\circ$  by  $3.75^\circ$  [Forget *et al.*, 2007] and are computed for a model layer 10 m above the

surface. This (and not a lower) elevation was chosen for several reasons: using model data for 0 m above the surface would be useless because technically, modelled wind is zero at the surface. It follows a log-law behaviour near the surface in accordance with the standard boundary layer theory of fluid flow [e.g. *Bagnold*, 1954; *Pye and Tsoar*, 1990]. Thus, data from 5 m above the surface, which is within the boundary layer, would not yield more information on the fluid flow itself than 10-m data. Higher elevation winds were chosen because the model does not map small-scale morphology. Some dune fields are several hundred meters high and thus not easily influenced by near-surface winds. Therefore, 10-m winds were used for wind data, which is representative enough for winds influencing all dunes. From the modelled data set, only the yearly maximum wind amplitudes and corresponding wind directions were used. The focus on yearly maximum wind data was intended to ensure that wind speeds are high enough to allow the lift of sand-sized particles. Wind direction data were computed in degree with respect to north direction and translated into geographical wind directions. Table 6 shows a part of the resultant wind speed and direction data set.

**Table 6:** Modelled yearly mean and maximum MCD wind direction (amplitude) and wind speed data (condensed abstract of the comprehensive database).

The model layer is 10 m above the surface. Data refer to the dust storm scenario during the dust storm season (Ls 180-360) when the highest wind speeds can be expected. Data were calculated for every individual crater locality. Locality IDs relate to the name of a crater, a regional location, or the name of a neighbouring crater. The data used for this analysis include yearly maximum wind direction and speed (bold).

dust storm scenario (10 m)			mean values for Ls 180 - 360			max values for Ls 180 - 360		
locality ID	LAT	LON (E)	mean wind amplitude [m/s]	wind direction [°]		maximum amplitude [m/s]	wind direction [°]	
Barnard	-61	41	7,1	151,41	SSE	19,74	<b>124,67</b>	<b>SE</b>
Elysium	9	63	5,4	115,08	ESE	11,85	<b>265,26</b>	<b>W</b>
Tyrrhena3	-6	65	6,01	10,33	N	13,62	<b>21,8</b>	<b>NNE</b>
Xante1	11	95	4,96	14,34	NNE	9,88	<b>2,04</b>	<b>N</b>
Cimmeria 1	-38	52	3,48	221,03	SW	6,34	<b>250,97</b>	<b>WSW</b>
Ma'adim Vallis	-23	16	5,78	298,81	WNW	13,22	<b>275,65</b>	<b>W</b>
Ophir 1	-2	98	5,62	336,42	NNW	14	<b>325,55</b>	<b>NW</b>
Marte Vallis	15	58	5,69	127,83	SE	12,05	<b>277,97</b>	<b>W</b>
Argyre 1	-44	23	5,86	87,52	E	13,37	<b>78,63</b>	<b>E</b>
Ophir 2	-7	76	6,57	8,26	N	16,16	<b>15,74</b>	<b>NNE</b>
Cimmeria 2	-38	13	6,12	62,36	ENE	15	<b>52,81</b>	<b>NE</b>
Thaumasia 1	-17	83	6,92	325,34	NW	12,68	<b>294,79</b>	<b>WNW</b>
Thaumasia 2	-16	1	5,03	291,63	WNW	11,74	<b>269,05</b>	<b>W</b>
Holden	-26	21	7,09	299,37	WNW	19,49	<b>278,63</b>	<b>W</b>
Fesenkov	21	91	8,17	45,98	NE	16,61	<b>63,89</b>	<b>ENE</b>
Nier	43	11	4,25	32,34	NNE	8,53	<b>343,22</b>	<b>NNW</b>
Gill	15	8	4,54	97,55	E	8,76	<b>312,47</b>	<b>NW</b>
Gill2	17	19	4,59	128,11	SE	9,69	<b>322,14</b>	<b>NW</b>
Kunowsky	57	8	3,99	15,38	NNE	10,11	<b>2,71</b>	<b>N</b>
Maraldi 2	-60	99	4,85	109,19	ESE	17,07	<b>104,15</b>	<b>ESE</b>
Perrotin	-2	85	4,98	7,64	N	9,4	<b>31,63</b>	<b>NNE</b>
Hesperia	-31	61	4,95	275,9	W	12,45	<b>282,25</b>	<b>WNW</b>
Melas Dorsa	-21	6	5,91	292,7	WNW	14,62	<b>276,57</b>	<b>W</b>
Tyrrhena 1	-14	34	6,27	328,13	NNW	14,49	<b>338,17</b>	<b>NNW</b>



### 4.7.2 Morphology-Deduced Wind Directions

Dunes, wind streaks, and wind shadow patterns are reliable indicators of the direction of the effective wind that creates the aeolian features. Especially the size of these features indicates the length of time for which the effective winds have been operating [Thomas and Gierasch, 1995]. Fig. 22 gives an overview of aeolian features and their corresponding effective wind directions. In this analysis, the dune slip face orientation was the major morphological feature used to determine the dune-building wind directions.

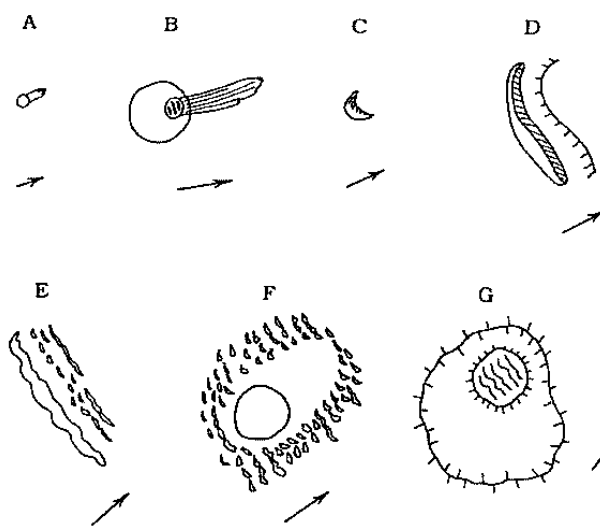


**Figure 22:** Aeolian features adequate for determining effective wind directions.

Wind directions are indicated by black arrows.

**A:** Crater-related wind streaks formed by enhanced erosion downwind of topographical obstacles. **B:** Type II streaks formed by the deflation of dark material deposits. **C:** Barchan or crescentic dune. **D:** Echo dune formed upwind of an obstacle. **E:** Farming dune formed on the upwind margin of dune fields. **F:** Dune field shadows, areas lacking dunes to the lee of obstacles caused by the diversion of sand flows and the increased complexity of the wind pattern. **G:** Intra-crater dune field usually formed on the downwind side of topographic depressions. [Thomas and Gierasch, 1995]

Data for morphology-deduced wind directions were created as azimuth vectors in the GIS by a visual analysis of the HRSC images. In a proportion of dune fields, it was helpful to use additional MOC NA image data sets (see Sect. 4.2) to resolve the dune slip faces and their orientation. In places where HRSC spatial resolution was insufficient to determine the slip face orientation and MOC data were missing, not every slip face orientation of the dune field could be determined. Where available, slip face orientation data from the Mars Global Digital Dune Database (MGD<sup>3</sup>, see below) were incorporated to complete the database of morphology-deduced wind directions for every crater locality.

The MGD<sup>3</sup> is a GIS-based database that provides a comprehensive quantitative view of the geographic distribution of dark dune fields on Mars [Hayward *et al.*, 2007a]. It is accessible via the internet at <http://pubs.usgs.gov/of/2007/1158/>. The nine layers of the database are available in ESRI shape file, ESRI geodatabase, and geography markup language (GML) formats [Hayward *et al.*, 2007b]. The MGD<sup>3</sup> currently covers a region from 65°N to 65°S and includes multiple parameters such as dune field area, estimated dune field volume, slip face orientation, average slip face, dune field centroid azimuth, crater centroid, GCM grid wind shear stress vectors, dune types, and many more

[*Hayward et al.*, 2007a]. Furthermore, additional image data sets such as THEMIS VIS and MOC NA are included. It was created to help researchers to examine the spatial distribution of aeolian features in a global context, compare their local features, understand global climatic and sedimentary processes, and locate areas of potential interest for local studies [*Hayward et al.*, 2007a; *Hayward et al.*, 2008]. The MGD<sup>3</sup> data sets used in this study are the 'raw slip face' ESRI shape files for a couple of dune fields, which are analyzed in this study as well as processed in the MGD<sup>3</sup>. This was particularly the case for the huge dune fields of Noachis Terra (e.g. Rabe Crater (43.9°S, 34.8°N), Russell Crater (54.9°S, 12.3°E), and Kaiser Crater (46.5°S, 18.8°E); see Fig. 2 and Appendix).

For a total of 14 localities, the MGD<sup>3</sup> slip face orientation data could be incorporated in this study. For the rest of the localities, slip face orientation shape files were created by the manual method mentioned above. Needless to say, no slip face orientation could be determined for the localities featuring only sand sheets and no dunes. These localities are marked with 'unknown wind direction'. It must be noted as well that for some dune fields more than one main wind direction could be deduced from the dune morphology whenever prevailing winds change seasonally. If at least one of these dune-building wind directions correlates with the GCM data, the locality is marked with 'partially concurred winds' (see analysis in Sect. 5.4). The azimuth vector shape files for every dune field were separately extracted into rose diagrams (Fig. 23). From these diagrams, the predominant wind direction for every dune field was easily assessable by direct reading.

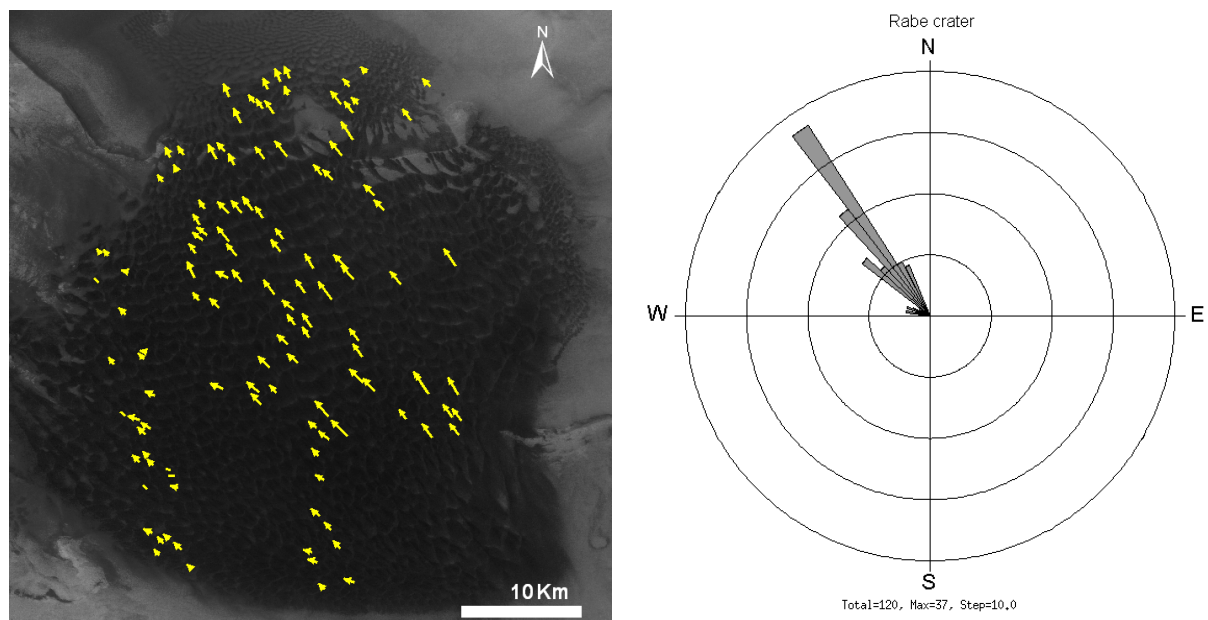


**Figure 23:** Morphology-deduced wind direction derived from slip-face orientation data: the Rabe Crater dune field example (43.9°S, 34.8°N).

**Left:** Part of the MDC<sup>3</sup> “raw\_slipface” shape file overlaid on HRSC 4280\_0000. The azimuths of the yellow arrows denote the downwind direction, as indicated by the dune slip faces. **Right:** Resultant rose diagram for the same dune field. The predominant wind direction towards the northeast is indicated by the great number of slip faces pointing in this direction.

## 4.8 The Resultant Database

The database for this study is founded on orbiter and model data for every locality collected and processed by the techniques described in the previous sections. Subject to availability, therefore, HRSC image and terrain information, MOC high-resolution image data, OMEGA spectral image data, THEMIS surface brightness temperature data, TES thermal inertia information, MOLA terrain information and modelled wind field data will be given for every locality. An overview of all datasets used can be found in a database in the Appendix.

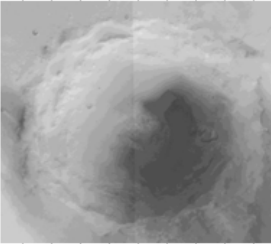
For each dark deposit analyzed, an HRSC preview image, the respective orbit or image number and ancillary orbit information such as observation season and solar longitude were stored in the database. Various parameters were measured and derived from the data sets collected. Compiled in the database, they provide a quick and clear overview of the localities. The exact locality of each crater in terms of latitude and longitude, the name of the region, the elevation of the floor and rim of the crater, its diameter and depth, the position of the dune field in the crater and its area were derived and determined from HRSC and MOLA terrain data. From this information, the size of dark deposits and craters as well as their location relative to others can be derived. The dune shapes used in morphological analyses were basically defined from HRSC and MOC high-resolution image data (see Sect. 4.2 and 4.7.2). Moreover, the modelled wind directions and those derived from dune slip-face orientation were incorporated in the database (Sect. 4.7) and used for the analysis described in Sect. 5.4. The results of the orbiter data analyses by the techniques described in Chapter V were assigned to the respective localities and incorporated in the database. These data cover the mineralogy of the dark deposits (Sect. 5.3) and their appearance in THEMIS image data as well as the respective surface brightness temperature values (Sect. 5.5.2), the thermal inertia of the dark deposits and the respective grain sizes (Sect. 5.5.3).

The following table summarizes all parameters analyzed and measured, assigning the respective data sets that were used to acquire these criteria.

**Table 7:** Overview of parameters measured for this analysis assigned to the respective data sets.

<b>Criterion/ Parameter</b>	<b>Crater Size, Elevation, Dune Position, Dune Shape</b>	<b>Thermal behaviour of dark material: compaction, grain size</b>	<b>Mineralogy</b>	<b>Slip face orientation</b>
<b>Data set</b>	HRSC, MOLA, MOC	THEMIS BTR TES TI	OMEGA	MDC <sup>3</sup> , MOC

Microsoft Excel is used to combine and save all this information, providing quick and effective access and orientation. Moreover, this tool permits analyzing the derived criteria statistically. Some of these analyses are presented in Chapter V. The complete database as well as the diagrams representing the statistical analyses are included in the Appendix. The spreadsheet of the database is entitled “Database”; the statistical spreadsheets are named after the respective calculation they relate to. The following table presents an extract of the database for one crater that is representative of the complete set of localities.

HRSC-ORBIT	Locality ID	Lat	Lon [E]	Lon [W]	Preview	Region	Crater Diameter [km]	Crater Diameter [m]	HRSC mean Altitude Crater Rim [m]	HRSC mean Altitude Crater Floor [m]	MOLA Altitude Crater Floor [m]	Crater Depth [m]	Crater Depth [km]	depth-diameter-ratio
0032_0000	Elysium	9,63	150,13	209,87		ELYSIUM PLANITIA	65	65000	-3503	-4343	-4068	840	0,84	0,013

Position of dark material in crater	HRSC Ls [°]	HRSC Season	OMEGA Orbit number	Omega Ls	Mineralogy	THEMIS with Ls [°]	Characteristic on THEMIS	BTR	Thermal Inertia	~ grain size	Moc Image Numbers	MCD wind direction	Wind Direction (from MOC, wind streaks, dune shape)
SW	335,77	N-summer	0032_3	335,77	pyroxene	115491026 (228.494°)		185	333	460			
							dark						
			1533_3	182,93	pyroxene	101699003 (7.259°)							
											E 1701373	W	

Dune Shapes / Distribution of Dark Material	Area of Dune Field [km2]	Comments
barchans on outer margin		
barchanoid in interior dune field	174,99	
sand sheet		

**Table 8:** Extract of the database (to be found in the Appendix) which covers one crater but is representative of the whole set of localities. The table should be read from left to right and is continued in each column. For every crater, a preview image, the orbiter data image numbers, the geographical location, ancillary measured parameters and the results of the various analyses are incorporated.